Physics of Fluids

RESEARCH ARTICLE | JUNE 03 2024

A high-order upwind compact difference scheme for solving the streamfunction-velocity formulation of the unsteady incompressible Navier–Stokes equations

Peixiang Yu (虞培祥) ; Bo Wang (王博) ; Hua Ouyang (欧阳华)

Physics of Fluids 36, 063601 (2024)
https://doi.org/10.1063/5.0209396

Physics of Fluids ARTICLE pubs.aip.org/aip/pof

A high-order upwind compact difference scheme for solving the streamfunction-velocity formulation of the unsteady incompressible Navier–Stokes equations

Cite as: Phys. Fluids **36**, 063601 (2024); doi: 10.1063/5.0209396
Submitted: 20 March 2024 · Accepted: 14 May 2024 ·
Published Online: 3 June 2024

Peixiang Yu (虞培祥),[1,2,a] Bo Wang (王博),[1] and Hua Ouyang (欧阳华)[1,2]

AFFILIATIONS

[1]School of Mechanical Engineering, Shanghai Jiao Tong University, Shanghai 200240, People's Republic of China
[2]Engineering Research Center of Gas Turbine and Civil Aero Engine, Ministry of Education, Shanghai 200240, People's Republic of China

[a)]Author to whom correspondence should be addressed: pxyu@sjtu.edu.cn

ABSTRACT

In this paper, we propose an upwind compact difference method with fourth-order spatial accuracy and second-order temporal accuracy for solving the streamfunction-velocity formulation of the two-dimensional unsteady incompressible Navier–Stokes equations. The streamfunction and its first-order partial derivatives (velocities) are treated as unknown variables. Three types of compact difference schemes are employed to discretize the first-order partial derivatives of the streamfunction. Specifically, these schemes include the fourth-order symmetric scheme, the fifth-order upwind scheme, and the sixth-order symmetric scheme derived by combining the two parts of the fifth-order upwind scheme. As a result, the fourth-order spatial discretization schemes are established for the Laplacian term, the biharmonic term, and the nonlinear convective term, along with the Crank–Nicolson scheme for the temporal discretization. The unconditional stability characteristic of the scheme for the linear model is proved by discrete von Neumann analysis. Moreover, six numerical experiments involving three test problems with the analytic solutions, and three flow problems including doubly periodic double shear layer, lid-driven cavity flow, and dipole-wall interaction are carried out to demonstrate the accuracy, robustness, and efficiency of the present method. The results indicate that the present method not only has good numerical performance but also exhibits quite efficiency.

I. INTRODUCTION

In the recent years, numerical methods for simulating incompressible fluid flows governed by Navier–Stokes (N–S) equations have been thoroughly investigated. Nowadays, the results obtained by the direct numerical simulation (DNS) without any turbulence models have been widely treated as the accurate solutions for the flow problems and have contributed to the study of flow mechanisms. In order to achieve high accuracy which is the essential requirement for DNS, it is necessary to develop high-order numerical methods. As the foundation of three-dimensional (3D) flow problems, algorithms for two-dimensional (2D) flow problems have also been widely studied in recent years. In this paper, we consider the following 2D unsteady N–S equations in the form of streamfunction-velocity formulation:

$$\frac{\partial}{\partial t}\left(\nabla^2\psi\right)+u\frac{\partial}{\partial x}\left(\nabla^2\psi\right)+v\frac{\partial}{\partial y}\left(\nabla^2\psi\right)=\frac{1}{Re}\nabla^4\psi+f,\qquad u=\frac{\partial\psi}{\partial y},\quad v=-\frac{\partial\psi}{\partial x},\tag{1}$$

where ψ is the streamfunction, u and v are the velocities, and Re is the Reynolds number. As the velocities can be regarded as the first-order partial derivatives of the streamfunction, the above formulation is also termed as the streamfunction-velocity formulation.

Compared with the traditional primitive variable formulation, there are at least three advantages of the above formulation. First, in the streamfunction-velocity formulation, the continuity equation which stands for mass conservation is automatically satisfied. Second, the velocity and pressure variables are decoupled, which overcomes

the difficulty in the solution of the pressure variables. Furthermore, the boundary conditions of the streamfunction are simpler than those of the pressure. Moreover, even compared with the streamfunction-vorticity formulation which is also widely used for the 2D incompressible fluid flow problems, the streamfunction-velocity formulation still has the unique advantage in the boundary condition setting. Therefore, in the past several years, many novel numerical methods based on the streamfunction-velocity formulation have been developed.[1–20]

Considering that the governing equation Eq. (1) is a fourth-order partial differential equation, the traditional second-order difference approach, which requires 13 points to discretize the equation, has to propose additional numerical boundary schemes. On the contrary, the compact scheme, which uses only the current grid points and eight neighbor points, does not require any additional numerical schemes. Thus, several compact schemes based on the streamfunction-velocity formulation have been proposed in the last few decades. Before 2010, several second-order compact finite difference methods have been proposed. For example, Kupferman[1] presented a two-step second-order scheme in 2002, in which the discretization of the advection term was based on the central-difference scheme with nonlinear slope limiters. In 2005, Ben-Artzi *et al.*[2] improved the above method and proposed another second-order central-difference conditional stable scheme. Kalita and Gupta[4] presented a one-step second-order implicit compact scheme in 2010. Since 2010, many researchers have focused on the establishment of high-order compact finite difference methods. For example, Ben-Artzi *et al.*[5] first proposed the fourth-order accurate schemes for the streamfunction-velocity formulation. Later, to extend the methods to complicated geometries, Sen and Kalita[12] presented a fourth-order essentially compact finite difference scheme in a conformal coordinate while Fishelov[14] presented a new fourth-order finite difference scheme directly in irregular domains. Recently, our team established a compact fourth-order scheme for the two-dimensional steady incompressible N–S equations in general curvilinear coordinates.[18]

Although the above algorithms have achieved success in solving the flow problems with smooth solutions, as mentioned in the work of Yu *et al.*,[16] the utilization of the central symmetric compact scheme for velocities might experience numerical oscillations in the strong shear flow problems due to its characteristic of no numerical dissipation. To overcome this deficiency, upwind schemes for the streamfunciton-velocity formulation have been developed. In 2018, Yu and Tian[16] first proposed a second-order upwind compact scheme for solving the streamfunction-velocity formulation of the incompressible N–S equations. Same as previous works,[1,2,5] the discretization of the viscous term used the combination of the streamfunction and its first derivative using a fourth-order symmetric compact scheme. However, a splitting method for the convective terms of the streamfunction-velocity formulation was introduced.[16] Thus, the upwind compact scheme for the approximation values of velocities can be utilized to calculate the convective terms. Recently, Lu *et al.*[21] established a new less time-consuming upwind compact scheme for the solution of the streamfunction-velocity formulation. Different from the work of Yu and Tian,[16] only the third-order upwind compact scheme for the first-order partial derivatives was required to be solved, while the fourth-order approximation of velocities was computed directly by the combination of those terms. Very recently, Yadav *et al.*[22] also developed a hybrid compact scheme for the streamfunction-velocity formulation of the incompressible N–S equations. In their work, the first-order spatial derivatives were approximated by an optimized upwind compact scheme, and the Laplacian and biharmonic operators were discretized using fourth-order hybrid compact schemes. For time discretization, the authors used an explicit fourth-stage fourth-order Runge–Kutta method and hybrid filters. Additionally, it is worth pointing out that all the above upwind schemes[16,21,22] can only reach second-order accuracy in space.

The purpose of this paper is to develop a high-order upwind compact difference algorithm for the streamfunction-velocity formulation of the 2D unsteady incompressible N–S equations. Similar to the work of Yu and Tian,[16] the first-order derivatives of streamfunction (velocities) are discretized by two schemes, namely, the fifth-order upwind compact difference scheme and the fourth-order symmetric compact difference scheme in this work. Referring to the strategy in the work of Lu *et al.*,[21] by the weighted combination of those numerical solutions, a sixth-order accurate value of the first-order derivatives can be obtained. Therefore, it is not necessary to solve another sixth-order scheme for the velocities to construct the high-order schemes such as in the work of Ben-Artzi *et al.*[5] By using the values of the streamfunction and its first-order derivatives, the fourth-order compact difference schemes for the convection and the biharmonic terms can be established. In addition, same as the previous work,[16,21] the Crank–Nicolson scheme is utilized for temporal discretization.

The remainder of this paper is organized as follows. In Sec. II, a high-order upwind compact difference algorithm for the streamfunction-velocity formulation of the unsteady incompressible N–S equations is deduced. In Sec. III, the stability analysis is provided for the linearized governing equation. Numerical experiments for six test problems are performed to validate the accuracy and efficiency of the newly derived compact difference scheme in Sec. IV. Finally, the whole work is summarized in Sec. V.

II. FOURTH-ORDER UPWIND COMPACT DIFFERENCE APPROXIMATION

A. Spatial discretization

In this section, we formulate a fourth-order upwind compact finite difference method that solves Eq. (1) in the uniform meshes with the grid size of h in the x- and y-directions. For brief sake, some standard finite difference operators at the grid point (x_i, y_j) are defined as follows:

$$\delta_x^2\delta_y\phi=\frac{\phi_{i+1,j+1}+\phi_{i-1,j+1}-\phi_{i-1,j-1}-\phi_{i+1,j-1}-2(\phi_{i,j+1}-\phi_{i,j-1})}{2h^3},$$

$$\delta_x\delta_y^2\phi=\frac{\phi_{i+1,j+1}-\phi_{i-1,j+1}-\phi_{i-1,j-1}+\phi_{i+1,j-1}-2(\phi_{i+1,j}-\phi_{i-1,j})}{2h^3},$$

$$\delta_x\delta_y\phi=\frac{\phi_{i+1,j+1}-\phi_{i-1,j+1}+\phi_{i-1,j-1}-\phi_{i+1,j-1}}{4h^2}, \tag{2}$$

$$\delta_x^2\phi=\frac{\phi_{i+1,j}-2\phi_{i,j}+\phi_{i-1,j}}{h^2},\quad \delta_x\phi=\frac{\phi_{i+1,j}-\phi_{i-1,j}}{2h},$$

$$\delta_y^2\phi=\frac{\phi_{i,j+1}-2\phi_{i,j}+\phi_{i,j-1}}{h^2},\quad \delta_y\phi=\frac{\phi_{i,j+1}-\phi_{i,j-1}}{2h},$$

where $\phi_{i,j}$ denotes the value at the grid point (x_i, y_j), etc.

1. The discretization of the first-order partial derivative

In the streamfunction-velocity formulation, it is essential to construct the appropriate scheme to calculate the approximal values of the first-order partial derivative of the streamfunction (velocity). For convenience, we would only use $u = \frac{\partial \psi}{\partial y}$ as an example. To establish the whole algorithm, three basic compact schemes are utilized

$$\hat{u}_{i,j-1} + 4\hat{u}_{i,j} + \hat{u}_{i,j+1} = \frac{3}{h}\left(\psi_{i,j+1} - \psi_{i,j-1}\right), \tag{3}$$

$$3\hat{u}^{+}_{i,j-1} + 6\hat{u}^{+}_{i,j} + \hat{u}^{+}_{i,j+1} = -\frac{1}{3h}\left(\psi_{i,j-2} + 18\psi_{i,j-1} - 9\psi_{i,j} - 10\psi_{i,j+1}\right), \tag{4}$$

$$\hat{u}^{-}_{i,j-1} + 6\hat{u}^{-}_{i,j} + 3\hat{u}^{-}_{i,j+1} = -\frac{1}{3h}\left(10\psi_{i,j-1} + 9\psi_{i,j} - 18\psi_{i,j+1} - \psi_{i,j+2}\right). \tag{5}$$

Equation (3) is the fourth-order symmetric compact difference scheme (SCD4), while Eqs. (4) and (5) are two parts of the fifth-order upwind compact difference scheme (UCD5).[23] Using the Taylor series expansion, we have

$$\hat{u} = \frac{\partial \psi}{\partial y} - \frac{h^4}{180}\frac{\partial^5 \psi}{\partial y^5} + O(h^6), \tag{6}$$

$$\hat{u}^{+} = \frac{\partial \psi}{\partial y} - \frac{h^5}{600}\frac{\partial^6 \psi}{\partial y^6} + \frac{h^6}{7000}\frac{\partial^7 \psi}{\partial y^7} + O(h^7), \tag{7}$$

$$\hat{u}^{-} = \frac{\partial \psi}{\partial y} + \frac{h^5}{600}\frac{\partial^6 \psi}{\partial y^6} + \frac{h^6}{7000}\frac{\partial^7 \psi}{\partial y^7} + O(h^7). \tag{8}$$

First, it should be pointed out that the fourth-order approximation $\hat{u}$ is critical for establishing the fourth-order discretization of the partial derivative $\frac{\partial^4 \psi}{\partial y^4}$. Considering u^* as an approximation of u with at least fourth-order accuracy, it can be expressed as follows:

$$u^* = \frac{\partial \psi}{\partial y} + \alpha h^4 \frac{\partial^5 \psi}{\partial y^5} + \beta h^5 \frac{\partial^6 \psi}{\partial y^6} + O(h^6). \tag{9}$$

In general, by employing Taylor series expansion and standard finite difference operators in Eq. (2), it yields

$$\delta_y^2 \psi = \frac{\partial^2 \psi}{\partial y^2} + \frac{h^2}{12}\frac{\partial^4 \psi}{\partial y^4} + \frac{h^4}{360}\frac{\partial^6 \psi}{\partial y^6} + O(h^6), \tag{10}$$

$$\delta_y u^* = \frac{\partial^2 \psi}{\partial y^2} + \frac{h^2}{6}\frac{\partial^4 \psi}{\partial y^4} + h^4\left(\frac{1}{120} + \alpha\right)\frac{\partial^6 \psi}{\partial y^6} + \beta h^5 \frac{\partial^7 \psi}{\partial y^7} + O(h^6). \tag{11}$$

Combining the above two equations and eliminating the second-order partial derivative term, we obtain

$$\frac{\partial^4 \psi}{\partial y^4} = \frac{12}{h^2}\left(\delta_y u^* - \delta_y^2 \psi\right) - 12h^2\left(\frac{1}{180} + \alpha\right)\frac{\partial^6 \psi}{\partial y^6} + 12\beta h^3 \frac{\partial^7 \psi}{\partial y^7} + O(h^4). \tag{12}$$

Note that the discretization of Eq. (12) can achieve fourth-order accuracy if $\alpha = -1/180$ and $\beta = 0$, and the SCD4 scheme satisfies this condition exactly. The above analysis indicates the true reason why SCD4 must be utilized in the whole algorithm.

Second, it also should be mentioned that more schemes are required to discretize the other partial derivatives of the streamfunction, especially for $\frac{\partial^3 \psi}{\partial y^3}$. Using the Taylor series expansion, we get

$$\begin{aligned}\delta_y^2 u^* &= \frac{\partial^2 u^*}{\partial y^2} + \frac{h^2}{12}\frac{\partial^4 u^*}{\partial y^4} + O(h^4) \\ &= \frac{\partial^3 \psi}{\partial y^3} + \frac{h^2}{12}\frac{\partial^5 \psi}{\partial y^5} + O(h^4),\end{aligned} \tag{13}$$

$$\begin{aligned}\delta_y \psi &= \frac{\partial \psi}{\partial y} + \frac{h^2}{6}\frac{\partial^3 \psi}{\partial y^3} + \frac{h^4}{120}\frac{\partial^5 \psi}{\partial y^5} + O(h^6) \\ &= u^* + \frac{h^2}{6}\frac{\partial^3 \psi}{\partial y^3} + h^4\left(\frac{1}{120} - \alpha\right)\frac{\partial^5 \psi}{\partial y^5} - \beta h^5 \frac{\partial^6 \psi}{\partial y^6} + O(h^6).\end{aligned} \tag{14}$$

Combing the above two equations to eliminate the term of $\frac{\partial^5 \psi}{\partial y^5}$, we can obtain the discretization scheme of $\frac{\partial^3 \psi}{\partial y^3}$ as follows:

$$\frac{\partial^3 \psi}{\partial y^3} = -\frac{3}{2}\delta_y^2 u^* + \frac{15}{h^2}\left(\delta_y \psi - u^*\right) + 15\alpha h^2 \frac{\partial^5 \psi}{\partial y^5} + 15\beta h^3 \frac{\partial^6 \psi}{\partial y^6} + O(h^4). \tag{15}$$

Obviously, to reach fourth-order accuracy for the partial derivative terms $\frac{\partial^3 \psi}{\partial y^3}$, the approximation scheme u^* must be at least six-order accuracy where α and β are both equal to 0. Consequently, other high-order schemes such as the sixth-order symmetric compact difference scheme should be introduced in the derivation of the fourth-order upwind method. Referring to the strategy in the work of Lu *et al.*,[21] we can combine the two parts of UCD5 to produce a new approximation of velocity with sixth-order accuracy

$$\bar{u} = \frac{\hat{u}^{+} + \hat{u}^{-}}{2}. \tag{16}$$

In this paper, the above approximation of velocity is called as the sixth-order weighted compact difference scheme (WCD6), and it can be deduced as

$$\bar{u} = \frac{\partial \psi}{\partial y} + \frac{h^6}{7000}\frac{\partial^7 \psi}{\partial y^7} + O(h^8). \tag{17}$$

2. The discretization of the biharmonic term

In this subsection, we discuss the fourth-order discretization for the biharmonic term

$$\nabla^4 \psi = \frac{\partial^4 \psi}{\partial x^4} + 2\frac{\partial^4 \psi}{\partial x^2 \partial y^2} + \frac{\partial^4 \psi}{\partial y^4}, \tag{18}$$

which stands for the viscous term in the N–S equations.

As mentioned in Sec. II A 1, we have

$$\frac{\partial^4 \psi}{\partial x^4} = \frac{12}{h^2}\left(-\delta_x \hat{v} - \delta_x^2 \psi\right) + O(h^4), \tag{19}$$

$$\frac{\partial^4 \psi}{\partial y^4} = \frac{12}{h^2}\left(\delta_y \hat{u} - \delta_y^2 \psi\right) + O(h^4). \tag{20}$$

For the fourth-order mixed partial derivative, referring to the previous publication,[5] it can be expressed as follows:

$$\frac{\partial^4\psi}{\partial x^2\partial y^2} = (3\delta_x^2\delta_y^2\psi + \delta_x\delta_y^2 v^* - \delta_x^2\delta_y u^*) + O(h^4). \tag{21}$$

Here, u^* and v^* are approximations of velocities u and v with at least fourth-order accuracy. We can choose $\bar{u}$ and $\bar{v}$ with sixth-order accuracy to replace u^* and v^*, respectively. Thus, the biharmonic term can be discretized as follows:

$$\begin{aligned}\nabla^4\psi = &\frac{12}{h^2}\left(-\delta_x\hat{v} + \delta_y\hat{u} - \delta_x^2\psi - \delta_y^2\psi\right)\\ &+ 2(3\delta_x^2\delta_y^2\psi + \delta_x\delta_y^2\bar{v} - \delta_x^2\delta_y\bar{u}) + O(h^4).\end{aligned} \tag{22}$$

3. The discretization of the convective term

Referring to our previous study,[16] the upwind formulation of the convective term can be written as follows:

$$\begin{aligned}&u\frac{\partial}{\partial x}(\nabla^2\psi) + v\frac{\partial}{\partial y}(\nabla^2\psi)\\ &= \frac{u+|u|}{2}\frac{\partial}{\partial x}(\nabla^2\psi)^+ + \frac{u-|u|}{2}\frac{\partial}{\partial x}(\nabla^2\psi)^-\\ &\quad + \frac{v+|v|}{2}\frac{\partial}{\partial y}(\nabla^2\psi)^+ + \frac{v-|v|}{2}\frac{\partial}{\partial y}(\nabla^2\psi)^-\\ &= \frac{u+|u|}{2}\nabla^2\left(\frac{\partial\psi}{\partial x}\right)^+ + \frac{u-|u|}{2}\nabla^2\left(\frac{\partial\psi}{\partial x}\right)^-\\ &\quad + \frac{v+|v|}{2}\nabla^2\left(\frac{\partial\psi}{\partial y}\right)^+ + \frac{v-|v|}{2}\nabla^2\left(\frac{\partial\psi}{\partial y}\right)^-\\ &= -\frac{u+|u|}{2}\nabla^2 v^+ - \frac{u-|u|}{2}\nabla^2 v^-\\ &\quad + \frac{v+|v|}{2}\nabla^2 u^+ + \frac{v-|v|}{2}\nabla^2 u^-.\end{aligned} \tag{23}$$

Here, u^+, u^-, v^+, and v^- represent the upwind terms of velocity. Additionally, in order to develop a fourth-order discretization of the convective term, all the velocity terms in Eq. (23) need to be at least fourth-order accuracy.

Now, we should pay attention to the high-order discretization of the harmonic terms. Using Taylor series expansion, we have

$$\begin{aligned}\delta_x^2 u^+ &= \frac{\partial^2 u}{\partial x^2} + \frac{h^2}{12}\frac{\partial^4 u}{\partial x^4} + O(h^4)\\ &= \frac{\partial^2 u}{\partial x^2} + \frac{h^2}{12}\frac{\partial^5\psi}{\partial x^4\partial y} + O(h^4).\end{aligned} \tag{24}$$

Noticing that

$$\begin{aligned}\delta_x^2\delta_y\psi &= \frac{\partial^3\psi}{\partial x^2\partial y} + \frac{h^2}{12}\frac{\partial^5\psi}{\partial x^4\partial y} + \frac{h^2}{6}\frac{\partial^5\psi}{\partial x^2\partial y^3} + O(h^4)\\ &= \frac{\partial^2 u}{\partial x^2} + \frac{h^2}{12}\frac{\partial^5\psi}{\partial x^4\partial y} + \frac{h^2}{6}\frac{\partial^5\psi}{\partial x^2\partial y^3} + O(h^4),\end{aligned} \tag{25}$$

$$\begin{aligned}\delta_x\delta_y v^* &= \frac{\partial^2 v}{\partial x\partial y} + \frac{h^2}{6}\frac{\partial^4 v}{\partial x^3\partial y} + \frac{h^2}{6}\frac{\partial^4 v}{\partial x\partial y^3} + O(h^4)\\ &= -\frac{\partial^3\psi}{\partial x^2\partial y} - \frac{h^2}{6}\frac{\partial^5\psi}{\partial x^4\partial y} - \frac{h^2}{6}\frac{\partial^5\psi}{\partial x^2\partial y^3} + O(h^4)\\ &= -\frac{\partial^2 u}{\partial x^2} - \frac{h^2}{6}\frac{\partial^5\psi}{\partial x^4\partial y} - \frac{h^2}{6}\frac{\partial^5\psi}{\partial x^2\partial y^3} + O(h^4).\end{aligned} \tag{26}$$

Combing Eqs. (24)–(26) to eliminate the $O(h^2)$ term, we can obtain

$$\frac{\partial^2 u}{\partial x^2} = \delta_x^2 u^+ + \delta_x^2\delta_y\psi + \delta_x\delta_y v^* + O(h^4). \tag{27}$$

On the other hand, we have

$$\begin{aligned}\delta_y^2 u^+ &= \frac{\partial^2 u}{\partial y^2} + \frac{h^2}{12}\frac{\partial^4 u}{\partial y^4} + O(h^4)\\ &= \frac{\partial^2 u}{\partial y^2} + \frac{h^2}{12}\frac{\partial^5\psi}{\partial y^5} + O(h^4).\end{aligned} \tag{28}$$

Noticing that

$$\hat{u} = \frac{\partial\psi}{\partial y} - \frac{h^4}{180}\frac{\partial^5\psi}{\partial y^5} + O(h^6), \tag{29}$$

$$\bar{u} = \frac{\partial\psi}{\partial y} + O(h^6). \tag{30}$$

It can be found that

$$\frac{\partial^5\psi}{\partial y^5} = \frac{180}{h^4}(\bar{u} - \hat{u}) + O(h^2). \tag{31}$$

Substituting Eq. (31) to Eq. (28), we have

$$\frac{\partial^2 u}{\partial y^2} = \delta_y^2 u^+ - \frac{15}{h^2}(\bar{u} - \hat{u}) + O(h^4). \tag{32}$$

Combing Eq. (27) and Eq. (32), the fourth-order discretization of $\nabla^2 u^+$ is given by

$$\begin{aligned}\nabla^2 u^+ &= \left(\frac{\partial^2 u}{\partial x^2}\right)^+ + \left(\frac{\partial^2 u}{\partial y^2}\right)^+\\ &= \delta_x^2 u^+ + \delta_y^2 u^+ + \delta_x^2\delta_y\psi + \delta_x\delta_y v^* - \frac{15}{h^2}(\bar{u} - \hat{u}) + O(h^4).\end{aligned} \tag{33}$$

Similarly, it can be deduced as

$$\begin{aligned}\nabla^2 u^- &= \delta_x^2 u^- + \delta_y^2 u^- + \delta_x^2\delta_y\psi + \delta_x\delta_y v^*\\ &\quad - \frac{15}{h^2}(\bar{u} - \hat{u}) + O(h^4),\end{aligned} \tag{34}$$

$$\begin{aligned}\nabla^2 v^+ &= \delta_x^2 v^+ + \delta_y^2 v^+ - \delta_x\delta_y^2\psi + \delta_x\delta_y u^*\\ &\quad - \frac{15}{h^2}(\bar{v} - \hat{v}) + O(h^4),\end{aligned} \tag{35}$$

$$\begin{aligned}\nabla^2 v^- &= \delta_x^2 v^- + \delta_y^2 v^- - \delta_x\delta_y^2\psi + \delta_x\delta_y u^*\\ &\quad - \frac{15}{h^2}(\bar{v} - \hat{v}) + O(h^4).\end{aligned} \tag{36}$$

As discussed in Sec. II A 1, the two parts of the UCD5 scheme can be utilized in the discretization of the upwind terms u^+, u^-, v^+ and v^-, and WCD6 scheme can be selected for the discretization of u and v. In addition, Substituting Eqs. (33)–(36) to Eq. (23), the discretization of the convective term can be expressed as follows:

$$
\begin{aligned}
&u\frac{\partial}{\partial x}(\nabla^2\psi)+v\frac{\partial}{\partial y}(\nabla^2\psi)\\
&=-\frac{\bar{u}+|\bar{u}|}{2}\left[\delta_x^2\hat{v}^+ +\delta_y^2\hat{v}^+ -\delta_x\delta_y^2\psi+\delta_x\delta_y\bar{u}-\frac{15}{h^2}(\bar{v}-\hat{v})\right]\\
&\quad-\frac{\bar{u}-|\bar{u}|}{2}\left[\delta_x^2\hat{v}^- +\delta_y^2\hat{v}^- -\delta_x\delta_y^2\psi+\delta_x\delta_y\bar{u}-\frac{15}{h^2}(\bar{v}-\hat{v})\right]\\
&\quad+\frac{\bar{v}+|\bar{v}|}{2}\left[\delta_x^2\hat{u}^+ +\delta_y^2\hat{u}^+ +\delta_x^2\delta_y\psi+\delta_x\delta_y\bar{v}-\frac{15}{h^2}(\bar{u}-\hat{u})\right]\\
&\quad+\frac{\bar{v}-|\bar{v}|}{2}\left[\delta_x^2\hat{u}^- +\delta_y^2\hat{u}^- +\delta_x^2\delta_y\psi+\delta_x\delta_y\bar{v}-\frac{15}{h^2}(\bar{u}-\hat{u})\right]+O(h^4)\\
&=-\frac{\bar{u}+|\bar{u}|}{2}\left(\delta_x^2\hat{v}^+ +\delta_y^2\hat{v}^+\right)-\frac{\bar{u}-|\bar{u}|}{2}\left(\delta_x^2\hat{v}^- +\delta_y^2\hat{v}^-\right)\\
&\quad+\frac{\bar{v}+|\bar{v}|}{2}\left(\delta_x^2\hat{u}^+ +\delta_y^2\hat{u}^+\right)+\frac{\bar{v}-|\bar{v}|}{2}\left(\delta_x^2\hat{u}^- +\delta_y^2\hat{u}^-\right)\\
&\quad+\left(\bar{u}\delta_x\delta_y^2\psi-\bar{u}\delta_x\delta_y\bar{u}+\bar{v}\delta_x^2\delta_y\psi+\bar{v}\delta_x\delta_y\bar{v}\right)\\
&\quad-\frac{15}{h^2}[\bar{v}(\bar{u}-\hat{u})-\bar{u}(\bar{v}-\hat{v})]+O(h^4).
\end{aligned}
\tag{37}
$$

B. Temporal discretization

Let ψ^n, u^n, and v^n denote the streamfunction at time t^n, we approximate Eq. (1) by the second-order Crank–Nicolson type scheme in time

$$
\begin{aligned}
&\frac{\nabla^2\psi^{n+1}-\nabla^2\psi^n}{\Delta t}\\
&\quad=-\frac{1}{2}\left[u\frac{\partial}{\partial x}(\nabla^2\psi)+v\frac{\partial}{\partial y}(\nabla^2\psi)-\frac{1}{Re}\nabla^4\psi-f\right]^{n+1}\\
&\qquad-\frac{1}{2}\left[u\frac{\partial}{\partial x}(\nabla^2\psi)+v\frac{\partial}{\partial y}(\nabla^2\psi)-\frac{1}{Re}\nabla^4\psi-f\right]^{n}+O(\Delta t^2),
\end{aligned}
\tag{38}
$$

where Δt is the uniform time step.

At the beginning, the harmonic term can be discretized as follows:

$$
\begin{aligned}
\nabla^2\psi&=\frac{\partial^2\psi}{\partial x^2}+\frac{\partial^2\psi}{\partial y^2}\\
&=2\delta_x^2\psi+2\delta_y^2\psi+\delta_x\bar{v}-\delta_y\bar{u}+O(h^4).
\end{aligned}
\tag{39}
$$

Substituting the spatial discretizations in Eqs. (22), (37), and (39) to the above semi-discretization equation in Eq. (38) and omitting the truncation error, we have the upwind compact discretization scheme with fourth-order spatial accuracy and second-order temporal accuracy for the streamfunction-velocity formulation

$$
\begin{aligned}
&\left(\frac{2}{\Delta t}+\frac{6}{Reh^2}\right)(\delta_x^2+\delta_y^2)\psi^{n+1}\\
&\quad=-\frac{1}{\Delta t}(\delta_x\bar{v}-\delta_y\bar{u})^{n+1}-\frac{1}{2}\left\{-\frac{\bar{u}+|\bar{u}|}{2}\left(\delta_x^2\hat{v}^+ +\delta_y^2\hat{v}^+\right)\right.\\
&\qquad-\frac{\bar{u}-|\bar{u}|}{2}\left(\delta_x^2\hat{v}^- +\delta_y^2\hat{v}^-\right)+\frac{\bar{v}+|\bar{v}|}{2}\left(\delta_x^2\hat{u}^+ +\delta_y^2\hat{u}^+\right)\\
&\qquad+\frac{\bar{v}-|\bar{v}|}{2}\left(\delta_x^2\hat{u}^- +\delta_y^2\hat{u}^-\right)-\frac{15}{h^2}(\bar{v}(\bar{u}-\hat{u})-\bar{u}(\bar{v}-\hat{v}))\\
&\qquad+\left(\bar{u}\delta_x\delta_y^2\psi-\bar{u}\delta_x\delta_y\bar{u}+\bar{v}\delta_x^2\delta_y\psi+\bar{v}\delta_x\delta_y\bar{v}\right)\\
&\qquad\left.-\frac{1}{Re}\left[\frac{12}{h^2}(-\delta_x\hat{v}+\delta_y\hat{u})+2(3\delta_x^2\delta_y^2\psi+\delta_x\delta_y^2\bar{v}-\delta_x^2\delta_y\bar{u})\right]-f\right\}^{n+1}\\
&\quad+\left(\frac{2}{\Delta t}-\frac{6}{Reh^2}\right)(\delta_x^2+\delta_y^2)\psi^n+\frac{1}{\Delta t}(\delta_x\bar{v}-\delta_y\bar{u})^n\\
&\quad-\frac{1}{2}\left\{-\frac{\bar{u}+|\bar{u}|}{2}\left(\delta_x^2\hat{v}^+ +\delta_y^2\hat{v}^+\right)-\frac{\bar{u}-|\bar{u}|}{2}\left(\delta_x^2\hat{v}^- +\delta_y^2\hat{v}^-\right)\right.\\
&\qquad+\frac{\bar{v}+|\bar{v}|}{2}\left(\delta_x^2\hat{u}^+ +\delta_y^2\hat{u}^+\right)+\frac{\bar{v}-|\bar{v}|}{2}\left(\delta_x^2\hat{u}^- +\delta_y^2\hat{u}^-\right)\\
&\qquad+\left(\bar{u}\delta_x\delta_y^2\psi-\bar{u}\delta_x\delta_y\bar{u}+\bar{v}\delta_x^2\delta_y\psi+\bar{v}\delta_x\delta_y\bar{v}\right)\\
&\qquad-\frac{15}{h^2}(\bar{v}(\bar{u}-\hat{u})-\bar{u}(\bar{v}-\hat{v}))-\frac{1}{Re}\left[\frac{12}{h^2}(-\delta_x\hat{v}+\delta_y\hat{u})\right.\\
&\qquad\left.\left.+2(3\delta_x^2\delta_y^2\psi+\delta_x\delta_y^2\bar{v}-\delta_x^2\delta_y\bar{u})\right]-f\right\}^{n}.
\end{aligned}
\tag{40}
$$

The matrix form of the algebraic system associated with the above algorithm can be written as follows:

$$
\Lambda\boldsymbol{\Psi}^{n+1}=\boldsymbol{F}(\boldsymbol{\Psi}^{n+1},\boldsymbol{U}^{n+1},\boldsymbol{V}^{n+1})+\boldsymbol{G}(\boldsymbol{\Psi}^{n},\boldsymbol{U}^{n},\boldsymbol{V}^{n}).
\tag{41}
$$

Noticing the coefficient matrix Λ is linear and positive definite, some traditional iterative methods such as the Gauss–Seidel method can be used to obtain the streamfunction at the $n+1$ time level.

C. Solution of the algebraic system

In this subsection, we provide the solution procedure of the algebraic systems arising from the newly proposed finite difference method. To improve the convergence for the streamfunction, the multigrid method is applied to solve the sparse linear systems arising from the approximations of the N–S equations in Eq. (41).

Suppose $\boldsymbol{\Psi}^n$, $\boldsymbol{U}^n$, $\boldsymbol{V}^n$ are known, the solutions of the $\boldsymbol{\Psi}^{n+1}$, $\boldsymbol{U}^{n+1}$, $\boldsymbol{V}^{n+1}$ are obtained by the following iterative procedure:

1. Set $k=0$ and initialize $\boldsymbol{\Psi}^{n+1,k}=\boldsymbol{\Psi}^n$, $\boldsymbol{U}^{n+1,k}=\boldsymbol{U}^n$, and $\boldsymbol{V}^{n+1,k}=\boldsymbol{V}^n$.
2. Calculate the right-hand side of Eq. (41) by using the values $\boldsymbol{\Psi}^{n+1,k}$, $\boldsymbol{U}^{n+1,k}$, $\boldsymbol{V}^{n+1,k}$, $\boldsymbol{\Psi}^n$, $\boldsymbol{U}^n$, and $\boldsymbol{\Psi}^n$.
3. Solve Eq. (41) using the V(3,3)-cycle multigrid method to obtain $\boldsymbol{\Psi}^{n+1,k+1}$.
4. Update the velocities such as $\boldsymbol{U}^{n+1,k+1}$ and $\boldsymbol{V}^{n+1,k+1}$ using Eqs. (3)–(5).
5. Repeat steps (2)–(4) from $k=1,2,3,\ldots$ until the maximum of $|\boldsymbol{\Psi}^{n+1,k+1}-\boldsymbol{\Psi}^{n+1,k}|$ is smaller than a certain inner convergence criterion ε (which constitutes the inner iteration). Then set $\boldsymbol{\Psi}^{n+1}=\boldsymbol{\Psi}^{n+1,k+1}$, $\boldsymbol{U}^{n+1}=\boldsymbol{U}^{n+1,k+1}$, $\boldsymbol{V}^{n+1}=\boldsymbol{V}^{n+1,k+1}$, etc.
6. Repeat steps (1)–(5) from $n=1,2,3,\ldots$ until the maximum of $|\boldsymbol{\Psi}^{n+1}-\boldsymbol{\Psi}^{n}|$ is smaller than a certain outer convergence criterion ε_s or to a certain time level (which constitute the outer iteration).

In this paper, all numerical simulations are run on a Dell OptiPlex 7070 machine with 32Gbyte of memory using double precision arithmetic.

III. LINEARIZED STABILITY ANALYSIS

Referring to the work,[16] we perform a von Neumann linear stability for the linearized homogeneous N–S equations

$$\frac{\partial}{\partial t}\left(\nabla^2\psi\right)+a\frac{\partial}{\partial x}\left(\nabla^2\psi\right)+b\frac{\partial}{\partial y}\left(\nabla^2\psi\right)=\frac{1}{Re}\nabla^4\psi, \tag{42}$$

where a and b are the corresponding mean values of u and v and are both real numbers.

We assume that the numerical solution at time level n can be expressed by the Fourier series, whose typical term is

$$\psi_0^n=\tilde{\psi}^n\exp(\mathrm{i}k_x x)\exp(\mathrm{i}k_y y), \tag{43}$$

where $\tilde{\psi}^n$ denotes the amplitude and k_x and k_y are the wave numbers in x- and y-directions respectively. Thus, the discrete Fourier modes for the velocities can be computed as follows:

$$\hat{v}=-\mathrm{i}\frac{3\sin\theta_x}{h(2+\cos\theta_x)}\psi_0^n, \tag{44}$$

$$\hat{u}=\mathrm{i}\frac{3\sin\theta_y}{h(2+\cos\theta_y)}\psi_0^n, \tag{45}$$

and

$$\begin{aligned}\hat{v}^+&=-\mathrm{i}\frac{189\sin\theta_x+54\sin2\theta_x+\sin3\theta_x}{6h(23+24\cos\theta_x+3\cos2\theta_x)}\psi_0^n\\&\quad-\frac{2(1-\cos\theta_x)^3}{3h(23+24\cos\theta_x+3\cos2\theta_x)}\psi_0^n\\&\triangleq-(\mathrm{i}k_{i,x}+k_{r,x})\psi_0^n,\end{aligned} \tag{46}$$

$$\begin{aligned}\hat{u}^+&=\mathrm{i}\frac{189\sin\theta_y+54\sin2\theta_y+\sin3\theta_y}{6h(23+24\cos\theta_y+3\cos2\theta_y)}\psi_0^n\\&\quad+\frac{2(1-\cos\theta_y)^3}{3h(23+24\cos\theta_y+3\cos2\theta_y)}\psi_0^n\\&\triangleq(\mathrm{i}k_{i,y}+k_{r,y})\psi_0^n,\end{aligned} \tag{47}$$

where $\theta_x=k_xh$ and $\theta_y=k_yh$ are phase angles in x- and y-directions, respectively. The other terms can be expressed as follows:

$$\hat{u}^-=(\mathrm{i}k_{i,y}-k_{r,y})\psi_0^n, \tag{48}$$

$$\hat{v}^-=-(\mathrm{i}k_{i,x}-k_{r,x})\psi_0^n, \tag{49}$$

$$\bar{u}=\mathrm{i}k_{i,y}\psi_0^n, \tag{50}$$

$$\bar{v}=-\mathrm{i}k_{i,x}\psi_0^n. \tag{51}$$

Applying the above equations, the spatial part of the unsteady term can be deduced as follows:

$$\begin{aligned}\nabla^2\psi&=\left(\frac{4(\cos\theta_x+\cos\theta_y-2)}{h^2}+\frac{\sin\theta_x\bar{k}_x+\sin\theta_y\bar{k}_y}{h}\right)\psi_0^n\\&\triangleq f_U(\theta_x,\theta_y,h)\psi_0^n,\end{aligned} \tag{52}$$

where $\bar{k}_x$ and $\bar{k}_y$ stand for the imaginary parts of modified wave numbers of $-\bar{v}$ and $\bar{u}$, and f_U is the real function.

Similarly, the Fourier modes for convective and viscous terms can be written as follows:

$$a\frac{\partial}{\partial x}\left(\nabla^2\psi\right)+b\frac{\partial}{\partial y}\left(\nabla^2\psi\right)=\left(\mathrm{i}\hat{f_C}(\theta_x,\theta_y,h)+f_C(\theta_x,\theta_y,h)\right)\psi_0^n, \tag{53}$$

$$\frac{1}{Re}\nabla^4\psi=f_V(\theta_x,\theta_y,h)\psi_0^n, \tag{54}$$

where $\hat{f_C}$, f_C, and f_V are real functions. Thus, the amplification factor $G(\theta_x,\theta_y)=\tilde{\psi}^{n+1}/\tilde{\psi}^n$ in the present scheme can be calculated as follows:

$$G=\frac{2f_U+\Delta t(f_V-f_C)-\mathrm{i}\Delta t\hat{f_C}}{2f_U-\Delta t(f_V-f_C)+\mathrm{i}\Delta t\hat{f_C}}. \tag{55}$$

In order to satisfy $|G(\theta_\xi,\theta_\eta)|\le1$, generally, it requires

$$\Delta t f_U(f_V-f_C)\le0. \tag{56}$$

It can be deduced as

$$\begin{aligned}f_U&=\frac{4(\cos\theta_x+\cos\theta_y-2)}{h^2}+\frac{\sin\theta_xk_x+\sin\theta_yk_y}{h}\\&=-\frac{308+277\cos\theta_x+16\cos2\theta_x-\cos3\theta_x}{3h^2(23+24\cos\theta_x+3\cos2\theta_x)}\sin^2\frac{\theta_x}{2}\\&\quad-\frac{308+277\cos\theta_y+16\cos2\theta_y-\cos3\theta_y}{3h^2(23+24\cos\theta_y+3\cos2\theta_y)}\sin^2\frac{\theta_y}{2}\le0.\end{aligned} \tag{57}$$

Therefore, the function of f_U is always non-positive.

For the function of f_C, assuming $a\ge0$ and $b\ge0$, since UCD5 scheme is applied to approximate u^+ and v^+, it yields

$$f_C=\frac{2(\cos\theta_x+\cos\theta_y-2)}{h^2}(ak_{r,x}+bk_{r,y})\le0, \tag{58}$$

because $(ak_{r,x}+bk_{r,y})$ is always positive in the upwind scheme.

For the function of f_V, it has

$$\begin{aligned}f_V&=\frac{1}{Re}\left[\frac{48}{h^4(2+\cos\theta_x)}\sin^4\frac{\theta_x}{2}+\frac{48}{h^4(2+\cos\theta_y)}\sin^4\frac{\theta_y}{2}\right.\\&\quad+\frac{4}{h^4}\left(6(\cos\theta_x-1)(\cos\theta_y-1)+(\cos\theta_x-1)\sin\theta_y\bar{k}_yh\right.\\&\quad\left.\left.+(\cos\theta_y-1)\sin\theta_x\bar{k}_xh\right)\right].\end{aligned} \tag{59}$$

It can be found that

$$\begin{aligned}&3(\cos\theta_x-1)(\cos\theta_y-1)+(\cos\theta_x-1)\sin\theta_y\bar{k}_yh\\&=(\cos\theta_x-1)\frac{(-207+72\cos\theta_y+136\cos2\theta_y-\cos3\theta_y)}{12(23+24\cos\theta_y+3\cos2\theta_y)}\ge0.\end{aligned} \tag{60}$$

Thus, f_V is also non-negative.

Combing the relationships of f_U, f_C, and f_V, it finally can be deduced as

$$f_U(f_V-f_C)\le0, \tag{61}$$

for the proposed scheme in this paper, which indicates that it is unconditionally stable for the linear model.

IV. NUMERICAL EXPERIMENTS

A. Taylor–Green vortex problem

First, we consider the Taylor–Green vortex problem, which has been widely used to evaluate the numerical performance of algorithms.[4,11,21,24] The analytical solutions are given as follows:

TABLE I. Comparison of L_2 norm errors, spatial convergence rates, and CPU time for Taylor–Green vortex problem at $t = 2$. Note: $4.94(-5) = 4.94 \times 10^{-5}$, etc.

		ψ		u		v		
Source	Grid size	Error	Rate	Error	Rate	Error	Rate	CPU time (s)
Present	31×31	4.94(−5)		1.16(−4)	4.92	1.16(−4)		44.9
	41×41	1.07(−5)	5.32	2.99(−5)	4.73	2.99(−5)	4.73	87.0
	51×51	3.32(−6)	5.23	1.09(−5)	4.54	1.09(−5)	4.54	158.3
Lu *et al.*[21]	31×31	2.38(−4)		4.34(−4)		4.34(−4)		13.8
	41×41	1.74(−4)	1.08	3.18(−4)	1.08	3.18(−4)	1.08	23.8
	51×51	1.26(−4)	1.47	2.28(−4)	1.49	2.28(−4)	1.49	42.2
	81×81	5.91(−5)	1.60	1.06(−4)	1.63	1.06(−4)	1.63	158.8

$$\psi(x, y, t) = \cos(Nx)\cos(Ny)\exp(-2N^2 t/\mathrm{Re})/N, \quad (62)$$

$$u(x, y, t) = -\cos(Nx)\sin(Ny)\exp(-2N^2 t/\mathrm{Re}), \quad (63)$$

$$v(x, y, t) = \sin(Nx)\cos(Ny)\exp(-2N^2 t/\mathrm{Re}), \quad (64)$$

where N is a given integer and equals to 2 in this problem. The computational domain is configured as a square region of size $0 \le x, y \le 2\pi$, while the initial and boundary conditions are all specified by the analytical solution in Eqs. (62)–(64). The convergence criterion of the inner iteration ε and the computation time t are set to 10^{-12} and 2, respectively. In addition, we also reproduce the codes of the less time-consuming second-order upwind compact scheme[21] for a better comparison.

Numerical simulations are first performed for cases with $Re = 100$ and $\Delta t = 0.01$ under different grid configurations. Table I comprehensively summarizes the L_2 norm errors, convergence rates, and CPU time for u, v, and ψ. As expected, the convergence rates of the present method are close to 4, which is in agreement with the theoretical derivation. In comparison with the results of the method,[21] although the present method requires more CPU computation time under the same grids, it shows higher efficiency in terms of obtaining results with the same level of accuracy. For example, our method yields the error of ψ equals to 4.94×10^{-5} under 31×31 grids, and the error of ψ for the method of Lu *et al.*[21] equals to 5.91×10^{-5} under 81×81 grids, which can be assumed to have the same level of accuracy. In terms of CPU time, our method requires 44.9 s under 31×31 grids, whereas the method of Lu *et al.* requires 158.8 s under 81×81 grids for the same level of accuracy. Therefore, the reduction in CPU time for our method is $(158.8 - 44.9)/158.8 \approx 72\%$ under the same level of accuracy conditions. In conclusion, our method achieves over 61% reduction in the grid requirement and 72% reduction in CPU time from the point of view that the results achieve the same level of accuracy. Furthermore, considering a grid size of 65×65 and $Re = 10$, the results for different Δt are presented in Table II, showing that the time convergence rates of our method approach 2, which is still consistent with theoretical derivations.

B. Analytical problem with a non-homogeneous source term

The second numerical experiment is a specially constructed smooth analytical solution with a non-homogeneous source term in the square domain $0 \le x, y \le 1$. The source term is given as follows:

$$f = -36e^{-t}(x^2 + y^2 + 16)(x^2 + y^2), \quad (65)$$

where the analytical solutions for $Re = 1$ can be expressed as follows:

$$\psi = e^{-t}(x^2 + y^2)^3, \quad (66)$$

$$u = 6e^{-t}y(x^2 + y^2)^2, \quad (67)$$

$$v = -6e^{-t}x(x^2 + y^2)^2. \quad (68)$$

To solve this problem, both the initial and boundary conditions are taken from the analytical solution, while ε and t are set to 10^{-12} and 1, respectively. Furthermore, we not only reproduce the codes in the work of Lu *et al.*[21] but also the codes in the work of Yu and Tian[16] for a more comprehensive comparison.

Table III presents the results under different grids with $\Delta t = 0.001$. Obviously, the spatial convergence rates of the present method are still close to four, once again proving fourth-order accuracy in space. Comparing the L_2 norm errors, it can be seen that our method has a great superiority in time-saving strategies by performing computation on sparser grids. Specifically, the L_2 norm errors of the present method under 21×21 grids are even smaller than those

TABLE II. Comparison of L_2 norm errors, temporal convergence rates, and CPU time for Taylor–Green vortex problem at $t = 2$.

		ψ		u		v		
Source	Δt	Error	Rate	Error	Rate	Error	Rate	CPU time (s)
Present	0.08	2.55 (−5)		4.31 (−5)		4.31 (−5)		151.5
	0.04	5.35 (−6)	2.25	9.63 (−6)	2.16	9.63 (−6)	2.16	193.7
	0.02	6.46 (−7)	3.05	1.85 (−6)	2.38	1.85 (−6)	2.38	271.9

TABLE III. Comparison of L_2 norm errors, spatial convergence rates, and CPU time for the analytical problem with a non-homogeneous source term at $t = 1$.

		ψ		u		v		
Source	Grid size	Error	Rate	Error	Rate	Error	Rate	CPU time(s)
Present	21×21	6.46 (−7)		4.88 (−6)		4.94 (−6)		198.7
	31×31	1.30 (−7)	3.96	9.73 (−7)	3.98	9.82 (−7)	3.98	994.8
	41×41	4.11 (−8)	3.99	3.09 (−7)	3.98	3.12 (−7)	3.99	2866.0
	51×51	1.65 (−8)	4.10	1.27 (−7)	3.98	1.28 (−7)	3.99	7615.0
Lu *et al.*[21]	21×21	8.88 (−5)		3.36 (−4)		3.29 (−4)		94.4
	31×31	4.45 (−5)	1.70	1.61 (−4)	1.81	1.59 (−4)	1.80	491.2
	41×41	2.66 (−5)	1.79	9.45 (−5)	1.86	9.32 (−5)	1.85	1430.1
	51×51	1.76 (−5)	1.84	6.20 (−5)	1.88	6.13 (−5)	1.88	3963.0
	81×81	7.27 (−6)	1.89	2.52 (−5)	1.92	2.50 (−5)	1.91	29 850.5
Yu and Tian[16]	21×21	4.65 (−5)		1.55 (−4)		1.54 (−4)		144.2
	31×31	2.04 (−5)	2.03	6.88 (−5)	2.00	6.84 (−5)	2.01	805.7
	41×41	1.15 (−5)	2.01	3.88 (−5)	1.99	3.86 (−5)	1.99	2475.9
	51×51	7.35 (−6)	2.00	2.49 (−5)	1.99	2.48 (−5)	1.99	6779.8
	81×81	2.88 (−6)	1.99	9.77 (−6)	1.99	9.72 (−6)	1.99	50 540.8

obtained by second-order upwind schemes[16,21] under 81×81 grids, where the grid reduction required to achieve the same level of accuracy is over 75%. In terms of CPU time, the present method shows an efficiency comparable to that of the second-order upwind method[16] under the same grid configurations. Compared with the fast upwind method,[21] the present method needs less than 1% CPU time from the view of achieving the same level of accuracy. In general, the present fourth-order method shows superior accuracy and efficiency even under sparse grids.

C. Analytical problem containing sharp boundary layers

Now, we consider the test problem containing sharp boundary layers,[8,25] which is a steady analytical solution of the N–S equations. The expressions for streamfunction and velocity are given as follows:

$$\psi(x,y) = \frac{(1-e^{-px})(1-e^{-py})}{(1-e^{-p})^2}, \tag{69}$$

$$u(x,y) = \frac{pe^{-py}(1-e^{-px})}{(1-e^{-p})^2}, \tag{70}$$

$$v(x,y) = -\frac{pe^{-px}(1-e^{-py})}{(1-e^{-p})^2}. \tag{71}$$

The source term is expressed as follows:

$$f(x,y) = \frac{1}{\mathrm{Re}}\frac{p^4(e^{-px}+e^{-py}-4e^{-px-py})}{(1-e^{-p})^2} + \frac{p^4e^{-px-py}(e^{-px}-e^{-py})}{(1-e^{-p})^4}, \tag{72}$$

where p is a key factor controlling the boundary layers, with larger values resulting in sharper boundary layers.

Here, we consider the case with $p = 50$ and $Re = 10$ in a square computational domain with $0 \le x, y \le 1$. In this case, there are sharp boundary layers near the sides $x = 0$ and $y = 0$ for streamfunction ψ, as well as near the sides $x = 0$ for v and $y = 0$ for u, respectively. Since the above solution in Eqs. (69)–(71) is a steady-state solution, we only use it to specify the boundary conditions, while the other regions are initialized with zero values. In addition, ε and ε_s are set to 10^{-8} and 10^{-9}, respectively. Δt is set to 0.0001, and grid configurations are 129×129.

Figure 1 displays the surface contours of streamfunction ψ. It can be observed that the second-order upwind methods[16,21] show larger errors, especially for the less time-consuming second-order upwind scheme,[21] while the present method can agree well with the analytical solution. In contrast with the maximal absolute errors in Table IV, the error magnitudes for our method are much smaller than those of the second-order upwind schemes. To better quantify the boundary layers capture performance, we depict the distribution of the streamfunction ψ and velocity u as well as the corresponding errors along the diagonal line in Fig. 2, it is obvious that the results obtained by the method[21] exhibit notable errors. Compared with the results of the method,[16] the present method demonstrates relatively smaller errors within the boundary layers, indicating a more accurate capture behavior of the sharp boundary layers. In summary, our fourth-order method exhibits superior performance under sparse grid configurations compared to second-order methods.

D. Doubly periodic double shear layer flow problem

The fourth numerical experiment focuses on the doubly periodic double shear layer flow problem, which has been widely adopted by scholars[16,21,24,26] to evaluate the numerical stability of the CFD algorithm at high wave numbers. Considering a square computational domain with sides of length 2π, the initial conditions are given as follows:

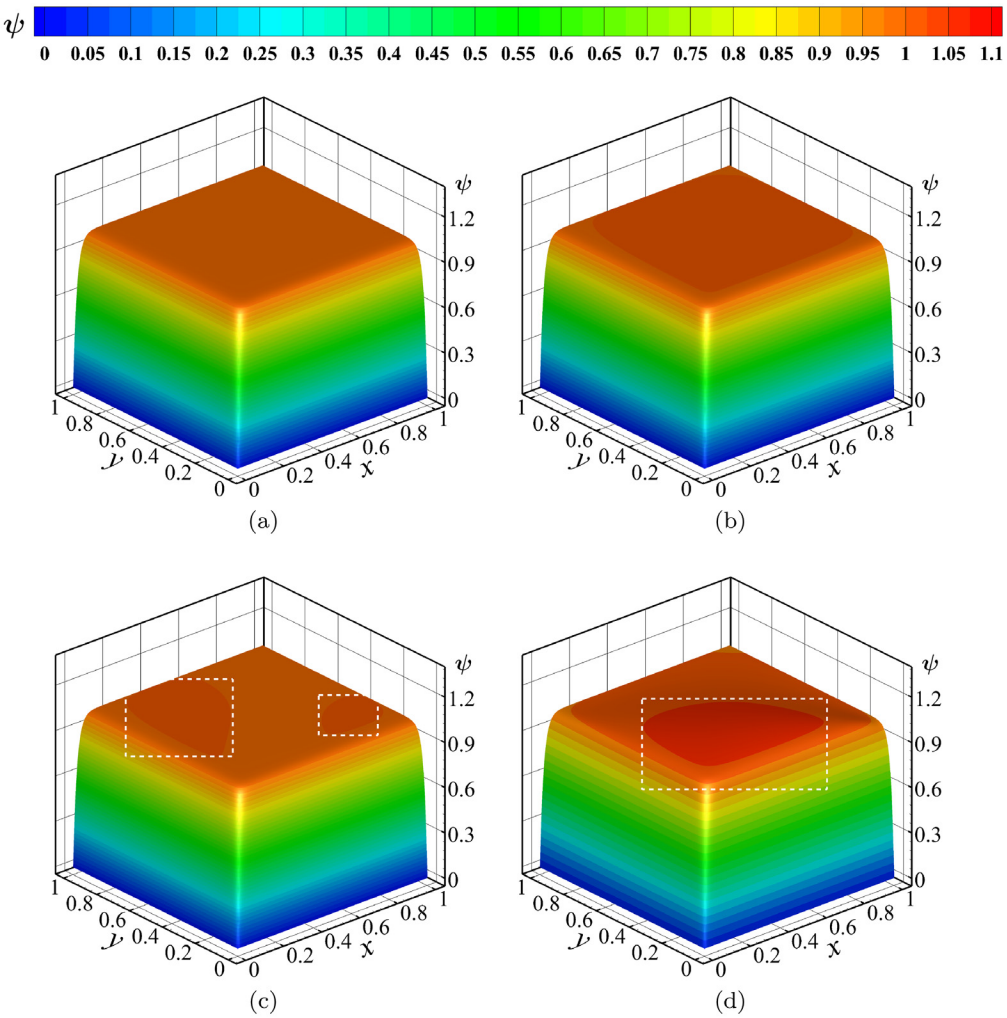

FIG. 1. The surface contours of $P = 50$, $Re = 10$ under 129×129 grids for streamfunction ψ for the analytical problem containing sharp boundary layers with (a) analytical solution, (b) present method, (c) Yu and Tian,[16] and (d) Lu *et al.*[21]

$$\psi(x,y,0) = \begin{cases} \rho \ln\cosh\left(\dfrac{2y-\pi}{2\rho}\right) - 2\rho \ln\cosh\left(\dfrac{\pi}{2\rho}\right) + \alpha\cos x, & 0 \le y \le \pi, \\ -\rho \ln\cosh\left(\dfrac{3\pi-2y}{2\rho}\right) + \alpha\cos x, & \pi \le y \le 2\pi, \end{cases} \tag{73}$$

$$u(x,y,0) = \begin{cases} \tanh\left(\dfrac{2y-\pi}{2\rho}\right), & 0 \le y \le \pi, \\ \tanh\left(\dfrac{3\pi-2y}{2\rho}\right), & \pi \le y \le 2\pi, \end{cases} \tag{74}$$

$$v(x,y,0) = \alpha \sin x. \tag{75}$$

TABLE IV. Comparison of maximal absolute error and CPU time for the analytical problem containing sharp boundary layers.

Grid size	Source	Maximal absolute error ψ	Maximal absolute error u	Maximal absolute error v	CPU time (s)
129×129	Present	6.44 (−4)	3.96 (−3)	5.47 (−3)	1703.5
	Yu and Tian[16]	1.11 (−3)	5.16 (−2)	3.31 (−2)	1116.9
	Lu *et al.*[21]	8.99 (−2)	5.27 (−1)	4.96 (−1)	650.5

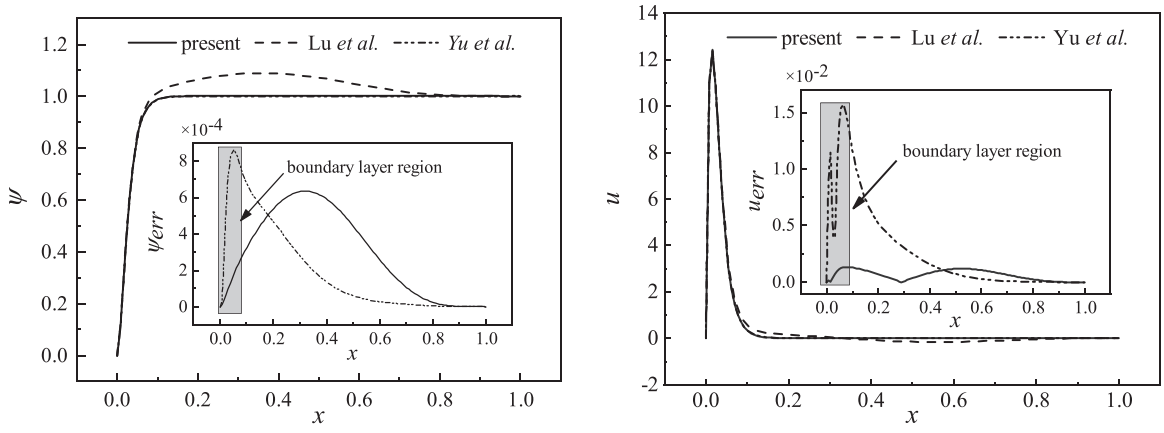

FIG. 2. The values and corresponding errors along the diagonal line for the analytical problem containing sharp boundary layers with (a) streamfunction ψ and (b) velocity u.

Here, $\rho = \pi/15$ is the thickness of the shear layer and $\alpha = 0.05$ is the initial perturbation. Periodic boundary conditions are applied along the four boundaries, which can be described as follows:

$$\phi(0, y, t) = \phi(2\pi, y, t), \quad \phi(x, 0, t) = \phi(x, 2\pi, t), \tag{76}$$

where ϕ represents the values of ψ, u, and v at the grid point.

For this problem, the increase in the Reynolds number will lead to the flow behavior with steep gradients. As mentioned in the work of Yu and Tian,[16] the central difference methods[4] may appear as serious nonphysical oscillations, while the upwind schemes could maintain acceptable performance. Additionally, in this numerical experiment, $Re = 10^4$, $\Delta t = 0.001$, and $\varepsilon = 10^{-8}$.

The comparisons of vorticity contours for different methods with the grid size of 129×129 are displayed in Fig. 3. It can be seen that both the second-order[4] and fourth-order[5] central difference schemes appear serious nonphysical oscillations, making it challenging to precisely capture the fine flow features. Although the fourth-order central difference method could partially reduce the numerical oscillations, the inherent non-dissipative characteristics of symmetric central difference schemes would still lead to severe numerical oscillation issues as time advances. In contrast, our fourth-order upwind scheme not only avoids the nonphysical oscillations but also accurately captures the fine flow features. Figure 4 presents the comparison results of u- velocity along the vertical centerline and v-velocity along the horizontal centerline at different time levels, and these results are all in good agreement with the well-established numerical solutions. Overall, for convection-dominated problems with high Reynolds numbers and large gradients, the fourth-order upwind scheme shows significant advantages.

E. The lid-driven square cavity flow problem

The lid-driven square cavity flow problem has been popular as a benchmark problem for assessing numerical methods due to its advantage of simple geometry for programing implementation and abundant fluid phenomena. For the steady incompressible viscous flow at low Reynolds numbers, scholars have obtained highly accurate numerical solutions.[16,21,27–31] For example, Marchi *et al.*[31] acquired the numerical results to the accuracy of the computational machine round-off error by second-order finite volume method under 8192×8192 grids and provided the variations of 11 selected variables across 38 Reynolds number values between 0.0001 and 10 000. Erturk *et al.*[29] obtained the accurate steady numerical solutions under 601×601 grids by the fourth-order compact scheme of streamfunction-vorticity formulation up to Reynolds number 20 000.

Considering a unit square computational domain, the upper wall moves at a constant velocity $u = 1$ while the other walls keep no-slip boundary conditions. ε and ε_s are set to 10^{-8} and 10^{-10}, $\Delta t = 0.001$. In addition, all simulations start from a zero initial field except for the upper wall. The kinetic energy is used as an evaluation metric, which is defined as follows:

$$E(t) = \int_{(x,y)\in[0,1]} \left[u(x, y, t)^2 + v(x, y, t)^2\right] dxdy. \tag{77}$$

To validate the accuracy of present methods without the analytical solution, we compute the cases for $Re = 1000$ and 3200. Table V lists the quantitative comparison results of primary vortex, which are in good agreement with these well benchmark solutions.[16,21,27–31] Taking the results of Marchi *et al.*[31] as the analytical solutions, it can be observed that the errors obtained by the present methods under 65×65 grids are even smaller than 6% and the spatial convergence rates in Table VI are close to 4. Again, all these results prove the accuracy and effectiveness of the present method.

For unsteady flow, Auteri *et al.*[32] found that there is a critical Reynolds number ($8017.6 \leq Re_{c1} \leq 8018.8$) for the first Hopf bifurcation, where the flow regime transitions from steady state to time periodicity, and the periodic flow transitions from time periodicity to quasi-periodicity at another critical Reynolds number ($9687 \leq Re_{c2} \leq 9765$) for the second Hopf bifurcation. However, different from the above findings, Kalita and Gupta[4] indicated the flow regime still keeps the time periodicity state for $Re = 10\,000$. In Fig. 5, we present the time-frequency characteristics diagrams for $Re = 10\,000$, which proves the flow is a periodic state rather than a quasi-periodic state, this conclusion is in agreement with the finding of Kalita and Gupta.[4] The period of a complete cycle is $T = 2.198$ while the corresponding frequency $f = 0.455$. Figure 6 presents the evolution of

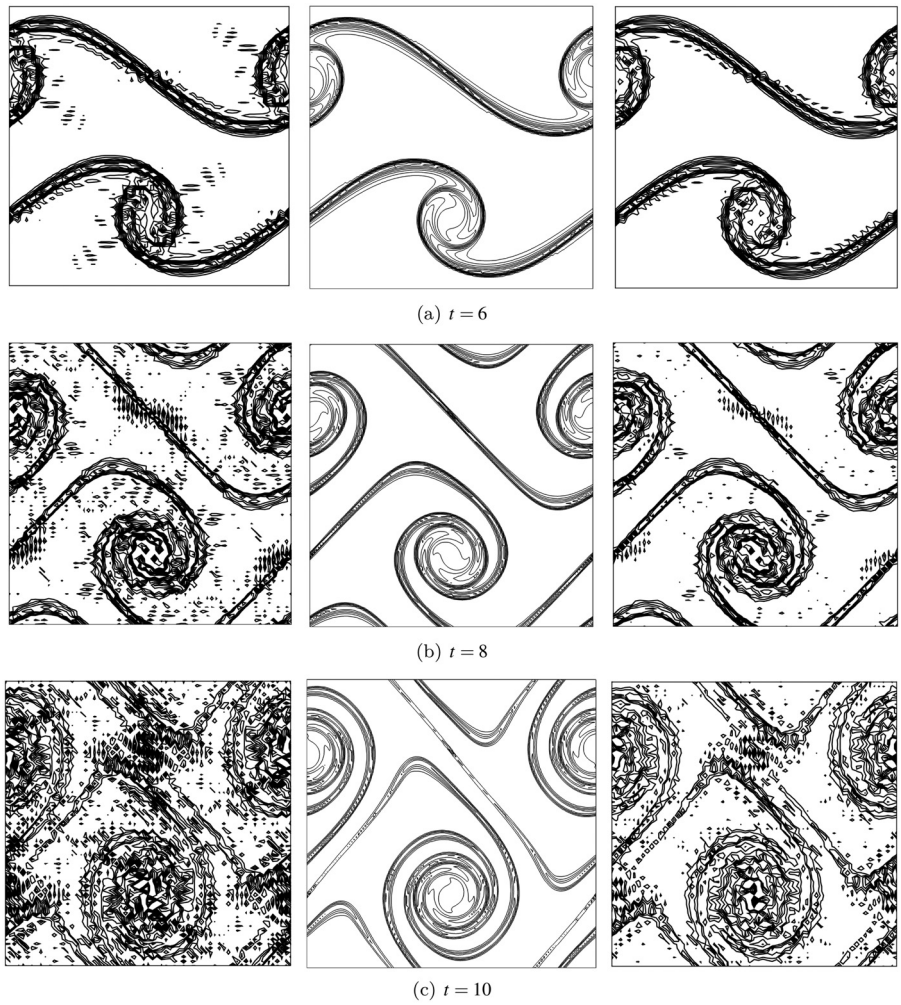

FIG. 3. The contours of vorticity under 129×129 grids for the second-order central difference method[4] (left), Present method (center), and fourth-order central difference method[5] (right) with (a) $t = 6$, (b) $t = 8$ and (c) $t = 10$. Reproduced with permission from Comput. Math. Appl. **75**, 3224 (2018). Copyright Elsevier.[16]

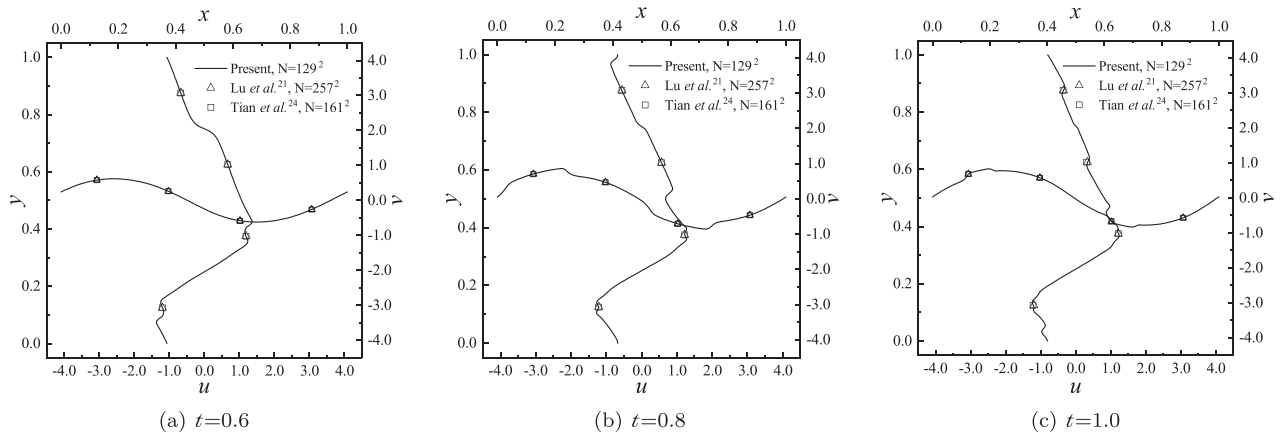

FIG. 4. Comparisons of the u-velocity along the vertical centerline and v-velocities along the horizontal centerline for the doubly periodic double shear layer problem with (a) $t = 0.6$, (b) $t = 0.8$, and (c) $t = 1.0$.

TABLE V. Comparison of the properties of primary vortex for the lid-driven square cavity flow problem for Re = 1000 and 3200.

Source	Grid size	Min(ψ)	Accuracy	x	y
		Re = 1000			
Present	65 × 65	−0.119 29	h^4	0.5313	0.5625
Ben-Artzi *et al.*[5]	65 × 65	−0.118 03	h^4	0.5313	0.5625
Ben-Artzi *et al.*[2]	81 × 81	−0.117 20	h^2	0.5250	0.5625
Present	129 × 129	−0.118 91	h^4	0.5313	0.5625
Yu and Tian[16]	129 × 129	−0.118 35	h^2	0.5313	0.5625
Lu *et al.*[21]	129 × 129	−0.118 42	h^2	0.5313	0.5625
Ghia *et al.*[27]	129 × 129	−0.117 93	h^2	0.5313	0.5625
Wahab *et al.*[30]	601 × 601	−0.118 94	h^4	0.5300	0.5660
Abdelmigid *et al.*[33]	601 × 601	−0.118 87	h^2	0.5308	0.5300
Erturk *et al.*[29]	601 × 601	−0.118 94	h^4	0.5300	0.5650
Marchi *et al.*[31]	8192 × 8192	−0.118 94	h^2	0.5308	0.5652
		Re = 3200			
Present	129 × 129	−0.122 46	h^4	0.5156	0.5391
Ghia *et al.*[27]	129 × 129	−0.120 38	h^2	0.5165	0.5469
Abdelmigid *et al.*[33]	601 × 601	−0.121 57	h^2	0.5175	0.5408
Marchi *et al.*[31]	8192 × 8192	−0.121 82	h^2	0.5179	0.5403

TABLE VI. Comparison of errors for the Min(ψ) and spatial convergence rates for the lid-driven square cavity flow problem.

	Re = 1000		Re = 3200	
Grid size	Error	Rate	Error	Rate
65 × 65	3.53(−4)		6.71(−3)	
129 × 129	2.68(−5)	3.72	6.42(−4)	3.39

streamlines for one main period, and it can be seen that the main feature of flow is no longer the appearance and disappearance of the tertiary vortexes for $Re = 8500$,[16] but a strong interaction of secondary, primary and tertiary vortexes, especially for the vortexes at the bottom left corner. At this Reynolds number, the instability of the flow is greatly increased and the flow phenomenon becomes very complex.

In general, benefiting from the advantage of spatial fourth-order accuracy and upwind scheme, the present method is demonstrated to be an effective tool for problems with high Reynolds numbers and relatively sparse grids.

F. Dipole–wall interaction problem

The dipole–wall interaction is taken from the works[34–36] as a benchmark for analyzing transient interactions between vortexes and walls in viscous incompressible flows. For this problem, as stressed by Tyliszczak,[36] this seemingly simple test case turned out to be

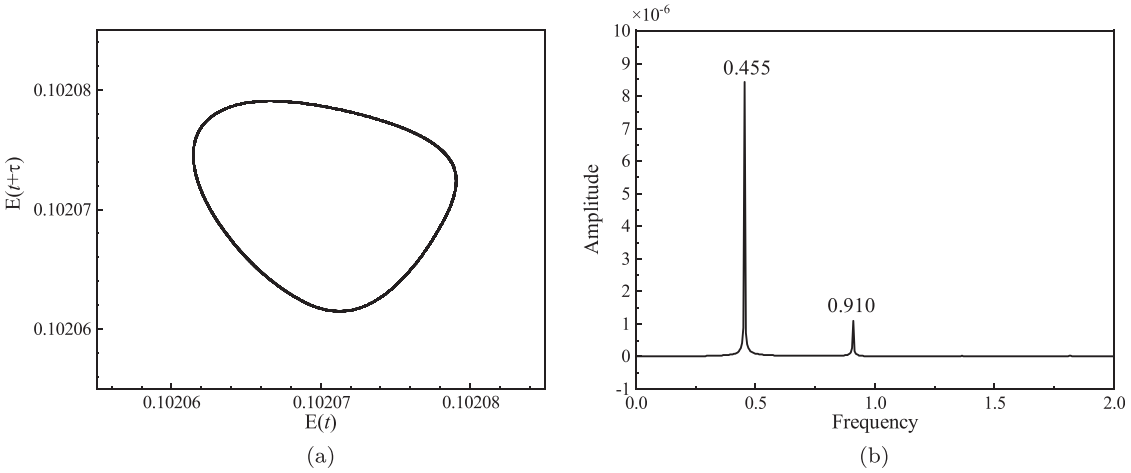

FIG. 5. Computed lid-driven square cavity flow of $Re = 10\,000$ with (a) phase portrait and (b) power spectrum of kinetic energy.

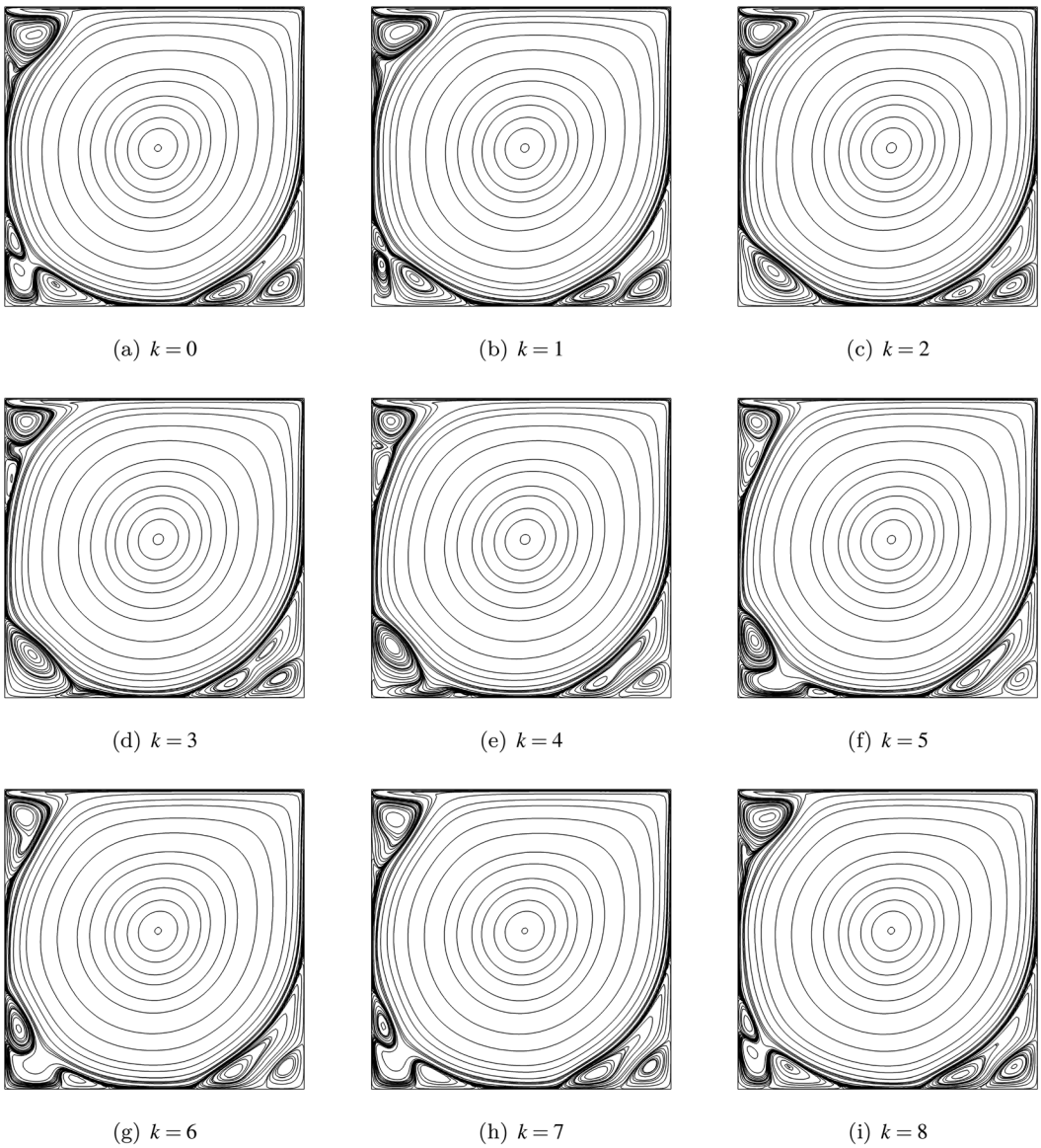

FIG. 6. Evolution of streamlines and the cyclic flow nature of one main period for the lid-driven square cavity flow at $t = t_0 + kT/8$ for $Re = 10\,000$ with (a) $k = 0$, (b) $k = 1$, (c) $k = 2$, (d) $k = 3$, (e) $k = 4$, (f) $k = 5$, (g) $k = 6$, (h) $k = 7$, and (i) $k = 8$.

extremely difficult from the point of view of achieving mesh-independent solutions. Due to the intense interaction initiated by the collision of dipoles with the wall, resulting in phenomena such as the fragmentation and deformation of vortexes, the wall grid resolution is crucial for accurately capturing the vortex morphology. We choose this particular case primarily to assess the ability of the present method to capture vortex morphology under uniformly sparse grid configurations.

The initial flow field is represented as two counter-rotating vortexes centered at the location $(x_1, y_1) = (0, 0.1)$ and $(x_2, y_2) = (0, -0.1)$. In the form of streamfunction-velocity, it can be expressed as follows:

$$u(x, y, 0) = -\frac{1}{2}\omega_e(y - y_1)\exp(-(r_1/r_0)^2) + \frac{1}{2}\omega_e(y - y_2)\exp(-(r_2/r_0)^2), \tag{78}$$

$$v(x, y, 0) = \frac{1}{2}\omega_e(x - x_1)\exp(-(r_1/r_0)^2) - \frac{1}{2}\omega_e(x - x_2)\exp(-(r_2/r_0)^2), \tag{79}$$

$$\psi(x, y, 0) = \frac{1}{4}\omega_e r_0^2(\exp(-(r_1/r_0)^2) - \exp(-(r_2/r_0)^2)), \tag{80}$$

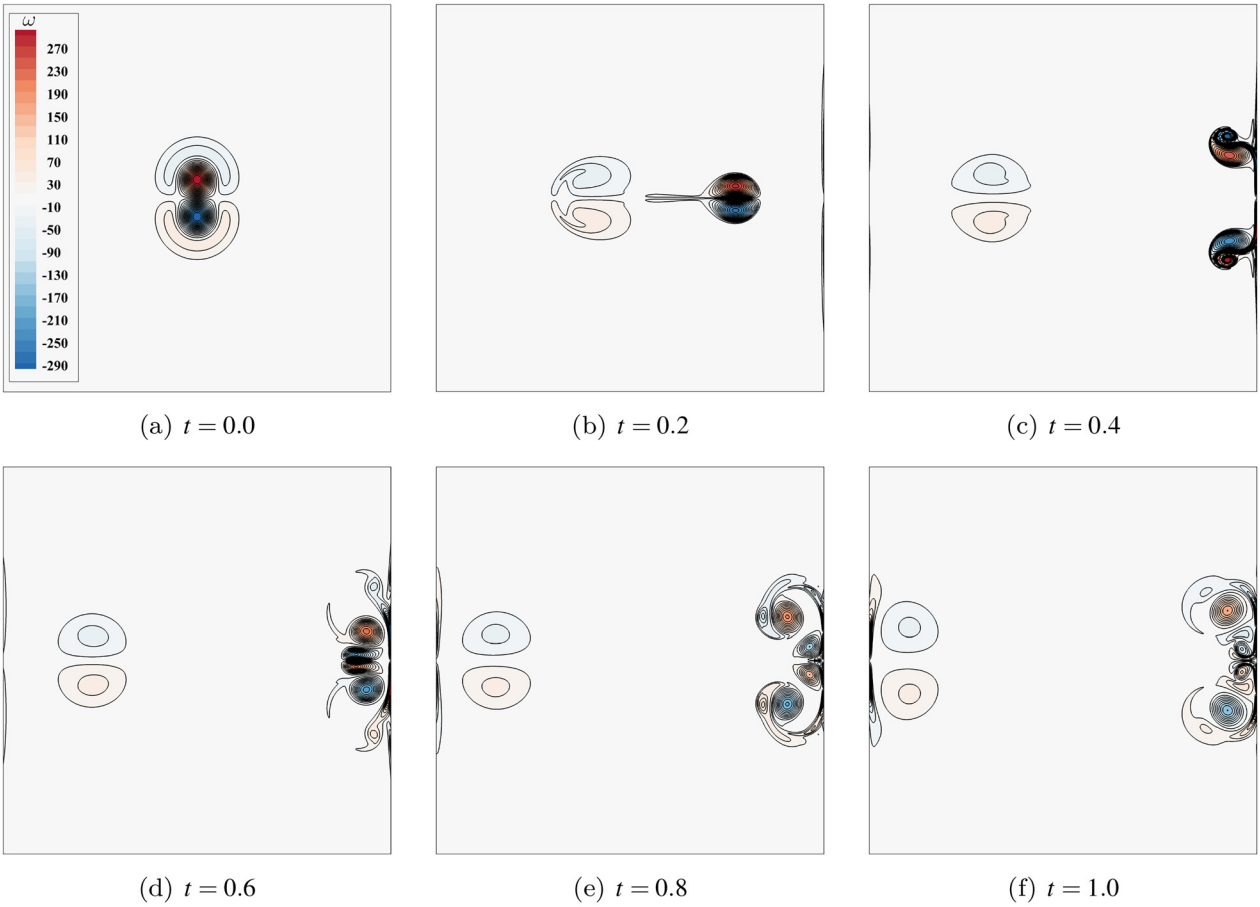

FIG. 7. Vorticity contours at selected time for Re = 1250 for dipole–wall interaction problem with (a) $t = 0.0$, (b) $t = 0.2$, (c) $t = 0.4$, (d) $t = 0.6$, (e) $t = 0.8$, and (f) $t = 1.0$.

where $r_0 = 0.1$ is the radius of the vortexes. $r_1 = \sqrt{(x - x_1)^2 + (y - y_1)^2}$ and $r_2 = \sqrt{(x - x_2)^2 + (y - y_2)^2}$ are the distance from the center of vortexes. ω_e is the extremum of vorticity at $r_{1,2} = 0$, which is set approximately to 300 according to Tyliszczak.[36]

In addition, the ε and Δt are set as 10^{-8} and 0.0001, respectively. The computation domain is configured as $-1 \le x, y \le 1$.

In Fig. 7, we present the vorticity contours at the selected time for $Re = 1250$. It can be observed that the vortexes undergo their first collision with the wall between the instance $t = 0.2$ and $t = 0.4$.

TABLE VII. A summary of the values for the first two maxims of the enstrophy for the dipole–wall interaction problem. Note: PS: pseudo-spectral method, FD-2nd: second-order finite difference method, FD-4th: fourth-order finite difference method.

Re	Source	Method	Grids	t_1	$\Omega(t_1)$	t_2	$\Omega(t_2)$
625	Present	FD-4th	257 × 257	0.371	949.5	0.657	301.2
	Present	FD-4th	513 × 513	0.371	924.5	0.648	303.9
	Tyliszczak[36]	FD-4th	512 × 512	0.374	881.6	0.653	302.6
	Tyliszczak[36]	FD-4th	1024 × 1024	0.371	931.4	0.648	305.0
	Clercx and Bruneau[34]	PS	256 × 256	0.371	933.6	0.648	305.2
	Clercx and Bruneau[34]	FD-2nd	1024 × 1024	0.371	932.8	0.647	305.2
1250	Present	FD-4th	257 × 257	0.343	2028.6	0.599	734.7
	Present	FD-4th	769 × 769	0.341	1880.8	0.616	721.2
	Clercx and Bruneau[34]	PS	384 × 384	0.341	1899.0	0.616	725.3
	Clercx and Bruneau[34]	FD-2nd	1536 × 1536	0.341	1891.0	0.616	724.9

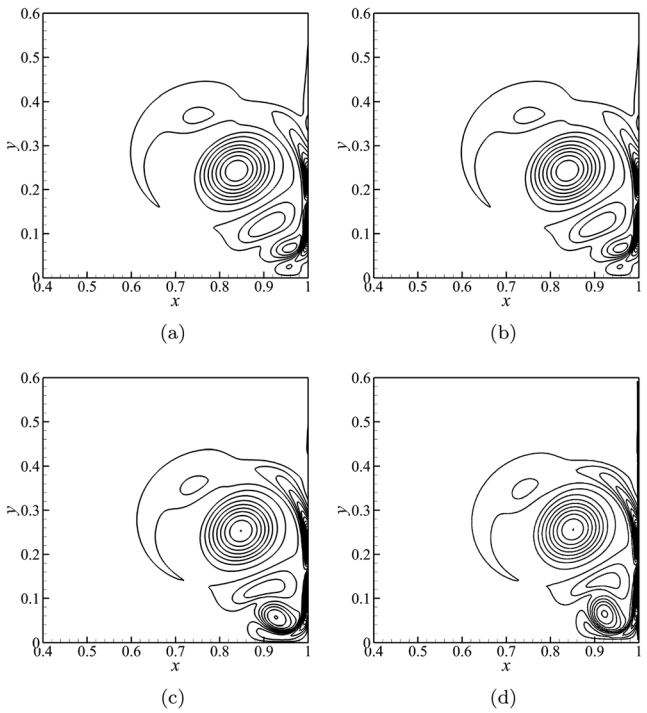

FIG. 8. Comparison of local vorticity contours at $t = 1$ under 513×513 grids for dipole–wall interaction problem with (a) Lu *et al.*,[21] (b) Yu and Tian,[16] (c) Present, and (d) Clercx and Bruneau.[34]

Subsequently, the post-collision vortexes experience another collision with the wall between $t = 0.6$ and $t = 0.8$, and the upper and lower vortexes consistently maintain a symmetrical shape in this process. Table VII tabulates a summary of the values for the first two maxims of the enstrophy, which corresponds to the two moments of dipole–wall collision. These quantitative results confirm the good agreement between our method and the benchmark solutions[34,36] even under spare grids. Additionally, the streamfunction-velocity method also demonstrates higher accuracy compared to the fourth-order pressure-velocity coupled projection method of Tyliszczak.[36] due to the advantages of velocity-pressure decoupling and more accurate boundary setting. A comparison of local vorticity contours at $t = 1$ under 513×513 grids is shown in Fig. 8, it can be seen that the second-order upwind methods[16,21] cannot accurately capture the vortex morphology near the horizontal line $y = 0$, while the results obtained by the present fourth-order upwind method are in good agreement with the vortex morphology of the benchmark solution obtained by the spectral method.[34]

Consider that there is no analytical solution to this problem, and the flow quantities vary significantly near the boundary layer and the center of the vortex. Data from specific grid points close to the center of the vortex in the upper right plane, available in all grid configurations, are extracted for convergence rates analysis. Taking the solution at $t = 1$ under 1025×1025 grids as the analytical solution, the results of spatial convergence rates are presented in Table VIII. It can be seen that even for the dramatic unsteady problem where the vortexes interact with the wall in a complex way, the convergence rates are still close to four. In general, the present high-order upwind method is an effective tool for capturing the dynamical behavior of complex small-scale vortexes.

V. CONCLUSIONS

In this paper, we develop an upwind compact difference method to solve the streamfunction-velocity formulation of the 2D unsteady incompressible N–S equations. By weighted combining the first-order partial derivatives of streamfunction (velocities) using different compact difference schemes to approximate the biharmonic and convective terms, we can deduce a fourth-order spatial accuracy upwind compact scheme. Discrete von Neumann linear stability analysis proves the present methods are unconditionally stable. Six numerical experiments involving three test problems with the analytic solutions, doubly periodic double shear layer flow problem, lid-driven square cavity flow problem, and dipole–wall interaction problem validate the accuracy, resolution, and efficiency of this newly proposed scheme.

Benefiting from the characteristic of fourth-order spatial accuracy, the present methods demonstrate to be less time-consuming by adopting sparse grids to achieve the same level of accuracy, which have high efficiency close to the second-order upwind scheme[16] under the same grids. In addition, the upwind property makes it

TABLE VIII. Comparison of absolute errors and spatial convergence rates for specific grid points (x_0, y_0) close to the center of the vortex in the upper-right plane for the dipole–wall interaction problem at $t = 1$. Note: $(x_0, y_0) = (0.804\,687\,5, 0.257\,812\,5)$ for $\mathrm{Re} = 625$, $(x_0, y_0) = (0.851\,562\,5, 0.257\,812\,5)$ for $\mathrm{Re} = 1250$.

		ψ			ω		
Re	Grid size	Value	Error	Rate	Value	Error	Rate
625	257	0.344 26	1.76(−3)	···	101.767 62	7.51(−1)	···
	513	0.345 82	1.95(−4)	3.17	102.448 65	6.37(−2)	3.55
	769	0.345 99	1.71(−5)	6.00	102.504 64	7.74(−3)	5.20
	1025	0.346 01	···	···	102.512 38	···	···
1250	257	0.399 00	6.58(−3)	···	146.377 47	2.36(1)	···
	513	0.406 29	7.09(−4)	3.22	169.005 44	9.67(−1)	4.61
	769	0.405 65	7.51(−5)	5.54	169.912 91	5.95(−2)	6.88
	1025	0.405 58	···	···	169.972 39	···	···

suitable for flow problems with large gradients and high Reynolds numbers.

Finally, it is worth pointing out that an extension of the present high-order upwind compact difference approach for the streamfunction-velocity formulation to the three-dimensional unsteady incompressible N–S equations as well as turbulent flow problems is under way.

ACKNOWLEDGMENTS

This work was supported in part by the National Science and Technology Major Project under Grant Nos. 2017-II-0007-0021 and J2019-II-0005-0025, and the Fundamental Research Funds for the Central Universities.

AUTHOR DECLARATIONS

Conflict of Interest

The authors have no conflicts to disclose.

Author Contributions

Peixiang Yu: Conceptualization (equal); Methodology (equal); Software (equal); Writing—original draft (equal); Writing—review & editing (equal). **Bo Wang:** Investigation (equal); Methodology (equal); Software (equal); Validation (equal); Writing—original draft (equal); Writing—review & editing (equal). **Hua Ouyang:** Supervision (equal); Writing—review & editing (equal).

DATA AVAILABILITY

The data that support the findings of this study are available from the corresponding author upon reasonable request.

REFERENCES

[1]R. Kupferman, "A central-difference scheme for a pure stream function formulation of incompressible viscous flow," SIAM J. Sci. Comput. **23**, 1–18 (2001).
[2]M. Ben-Artzi, J.-P. Croisille, D. Fishelov, and S. Trachtenberg, "A pure-compact scheme for the streamfunction formulation of Navier–Stokes equations," J. Comput. Phys. **205**, 640–664 (2005).
[3]M. M. Gupta and J. C. Kalita, "A new paradigm for solving Navier–Stokes equations: Streamfunction-velocity formulation," J. Comput. Phys. **207**, 52–68 (2005).
[4]J. C. Kalita and M. M. Gupta, "A streamfunction-velocity approach for 2D transient incompressible viscous flows," Int. J. Numer. Methods Fluids **62**, 237–266 (2010).
[5]M. Ben-Artzi, J.-P. Croisille, and D. Fishelov, "A high order compact scheme for the pure-streamfunction formulation of the Navier–Stokes equations," J. Sci. Comput. **42**, 216–250 (2010).
[6]Z. F. Tian and P. X. Yu, "An efficient compact difference scheme for solving the streamfunction formulation of the incompressible Navier–Stokes equations," J. Comput. Phys. **230**, 6404–6419 (2011).
[7]P. X. Yu and Z. F. Tian, "Compact computations based on a stream-function–velocity formulation of two-dimensional steady laminar natural convection in a square cavity," Phys. Rev. E **85**, 036703 (2012).
[8]P. X. Yu and Z. F. Tian, "A compact streamfunction-velocity scheme on non-uniform grids for the 2D steady incompressible Navier–Stokes equations," Comput. Math. Appl. **66**, 1192–1212 (2013).
[9]P. X. Yu and Z. F. Tian, "A compact scheme for the streamfunction-velocity formulation of the 2D steady incompressible Navier–Stokes equations in polar coordinaes," J. Sci. Comput. **56**, 165–189 (2013).
[10]P. X. Yu, J. X. Qiu, Q. Qin, and Z. F. Tian, "Numerical investigation of natural convection in a rectangular cavity under different directions of uniform magnetic field," Int. J. Heat Mass Transfer **67**, 1131–1144 (2013).
[11]S. Sen, J. C. Kalita, and M. M. Gupta, "A robust implicit compact scheme for two-dimensional unsteady flows with a biharmonic stream function formulation," Comput. Fluids **84**, 141–163 (2013).
[12]S. Sen and J. C. Kalita, "A 4OEC scheme for the biharmonic steady Navier–Stokes equations in non-rectangular domains," Comput. Phys. Commun. **196**, 113–133 (2015).
[13]S. Pandit and H. Karmakar, "An efficient implicit compact streamfunction velocity formulation of two dimensional flows," J. Sci. Comput. **68**, 653–688 (2016).
[14]D. Fishelov, "A new fourth-order compact scheme for the Navier–Stokes equations in irregular domains," Comput. Math. Appl. **74**, 6–25 (2017).
[15]P. Yu, Z. F. Tian, A. Y. Ying, and M. A. Abdou, "Stream function-velocity-magnetic induction compact difference method for the 2D steady incompressible full magnetohydrodynamic equations," Comput. Phys. Commun. **219**, 45–69 (2017).
[16]P. Yu and Z. F. Tian, "An upwind compact difference scheme for solving the streamfunction-velocity formulation of the unsteady incompressible Navier–Stokes equation," Comput. Math. Appl. **75**, 3224–3243 (2018).
[17]P. Yu and Z. F. Tian, "A high-order compact scheme for the pure streamfunction (vector potential) formulation of the 3D steady incompressible Navier–Stokes equations," J. Comput. Phys. **382**, 65–85 (2019).
[18]J. Q. Chen, P. Yu, Z. F. Tian, and H. Ouyang, "A high-order compact scheme for solving the 2D steady incompressible Navier–Stokes equations in general curvilinear coordinates," Int. J. Numer. Methods Fluids **92**, 456–477 (2020).
[19]Z. C. Xiao, P. Yu, H. Ouyang, and J. J. Zhang, "A parallel high-order compact scheme for the pure streamfunction formulation of the 3D unsteady incompressible Navier–Stokes equation," Commun. Nonlinear Sci. Numer. Simul. **95**, 105631 (2021).
[20]B. Peng, X. H. Guo, Y. Zu, and Z. F. Tian, "A physics-preserving pure streamfunction formulation and high-order compact solver with high-resolution for three-dimensional steady incompressible flows," Phys. Fluids **35**, 043104 (2023).
[21]J. B. Lu, Z. X. Chen, and Z. F. Tian, "A less time-consuming upwind compact difference method with adjusted dissipation property for solving the unsteady incompressible Navier–Stokes equations," Comput. Math. Appl. **126**, 149–171 (2022).
[22]V. S. Yadav, V. Maurya, P. K. Maurya, and M. K. Rajpoot, "Novel hybrid compact schemes for stream function-velocity formulation of the incompressible Navier–Stokes equations," Phys. Fluids **35**, 017114 (2023).
[23]M. H. Carpenter, D. Gottlieb, and S. Abarbanel, "The stability of numerical boundary treatments for compact high-order finite-difference schemes," J. Comput. Phys. **108**, 272–295 (1993).
[24]Z. F. Tian, X. Liang, and P. X. Yu, "A higher order compact finite difference algorithm for solving the incompressible Navier–Stokes equations," Int. J. Numer. Methods Eng. **88**, 511–532 (2011).
[25]J. Wang, W. J. Zhong, and J. Zhang, "High order compact computation and nonuniform grids for streamfunction vorticity equations," Appl. Math. Comput. **179**, 108–120 (2006).
[26]J. B. Bell, P. Colella, and H. M. Glaz, "A second-order projection method for the incompressible Navier–Stokes equations," J. Comput. Phys. **85**, 257–283 (1989).
[27]U. Ghia, K. Ghia, and C. Shin, "High-Re solutions for incompressible flow using the Navier–Stokes equations and a multigrid method," J. Comput. Phys. **48**, 387–411 (1982).
[28]N. Wright and P. Gaskell, "An efficient multigrid approach to solving highly recirculating flows," Comput. Fluids **24**, 63–79 (1995).
[29]E. Erturk and C. Gökçöl, "Fourth-order compact formulation of Navier–Stokes equations and driven cavity flow at high Reynolds numbers," Int. J. Numer. Methods Fluids **50**, 421–436 (2006).
[30]E. M. Wahba, "Steady flow simulations inside a driven cavity up to Reynolds number 35,000," Comput. Fluids **66**, 85–97 (2012).
[31]C. H. Marchi, C. D. Santiago, and C. A. R. D. Carvalho, Jr.,"Lid-driven square cavity flow: A benchmark solution with an 8192 × 8192 grid," J. Verif. Validation Uncertainty **6**, 041004 (2021).

[32]F. Auteri, N. Parolini, and L. Quartapelle, "Numerical investigation on the stability of singular driven cavity flow," J. Comput. Phys. **183**, 1–25 (2002).
[33]T. A. Abdelmigid, K. M. Saqr, M. A. Kotb, and A. A. Aboelfarag, "Revisiting the lid-driven cavity flow problem: Review and new steady state benchmarking results using GPU accelerated code," Alexandria Eng. J. **56**, 123–135 (2017).
[34]H. J. H. Clercx and C. H. Bruneau, "The normal and oblique collision of a dipole with a no-slip boundary," Comput. Fluids **35**, 245–279 (2006).
[35]R. Knikker, "Study of a staggered fourth-order compact scheme for unsteady incompressible viscous flows," Int. J. Numer. Methods Fluids **59**, 1063–1092 (2009).
[36]A. Tyliszczak, "A high-order compact difference algorithm for half-staggered grids for laminar and turbulent incompressible flows," J. Comput. Phys. **276**, 438–467 (2014).